Preventing alternans-induced spiral wave breakup in cardiac tissue: An ion-channel-based approach

D. Allexandre
Department of Biomedical Engineering, Case Western Reserve University, Cleveland, Ohio 44106, USA

N. F. Otani*
Department of Biomedical Sciences, Cornell University, Ithaca, New York 14853, USA
(Received 12 March 2004; published 3 December 2004)

The detailed processes involved in spiral wave breakup, believed to be one major mechanism by which tachycardia evolves into fibrillation, are still poorly understood. This has rendered difficult the proper design of an efficient and practical control stimulus protocol to eliminate such events. In order to gain new insights into the underlying electrophysiological and dynamical mechanisms of breakup, we applied linear perturbation theory to a steadily rotating spiral wave in two spatial dimensions. The tissue was composed of cells modeled using the Fenton-Karma equations whose parameters were chosen to emphasize alternans as a primary mechanism for breakup. Along with one meandering mode, not just one but several unstable alternans modes were found with differing growth rates, frequencies, and spatial structures. As the conductance of the fast inward current was increased, the instability of the modes increased, consistent with increased meandering and propensity for spiral breakup in simulations. We also explored a promising new approach, based on the theory, for the design of an energy efficient electrical stimulus protocol to control spiral wave breakup. The novelty lies in addressing the problem directly at the ion channel level and taking advantage of the inherent two dimensional nature of the rotating wave. With the help of the eigenmode method, we were able to calculate the exact timing and amplitude of the stimulus, and locate it optimally to maximize efficiency. The analysis led to a special-case example that demonstrated that a single, properly timed stimulus can have a global effect, suppressing all growing alternans modes over the entire tissue, thus inhibiting spiral wave breakup.

DOI: 10.1103/PhysRevE.70.061903 PACS number(s): 87.19.Hh, 05.10.−a, 87.17.Aa, 87.18.Bb

I. INTRODUCTION

Ventricular fibrillation remains one of the leading immediate causes of sudden cardiac death in North America [1]. Yet, despite extensive research, its nature as well as the electrophysiological mechanisms responsible for its initiation and sustenance are still not fully understood. In the structurally normal heart, recent experimental and theoretical research suggest that the breakup of a single stationary or meandering spiral or scroll wave into multiple reentrant waves may be one of the major mechanisms underlying fibrillation [2–5]. However, the conditions during which breakup occurs are still the source of much debate [6–10]. In particular, mechanisms involving alternans (i.e., beat-to-beat alternation in action potential duration) as an important cause of breakup, are still the subject of much research and discussion [8–15].

A number of approaches have been taken in the investigation of spiral wave dynamics and wave breakup. One approach consists of direct computer simulation of the partial differential equations (PDEs) governing the dynamics [2,11,16–25]. The analysis performed often reveals how the dynamics are modified when certain properties of the cells and/or tissue (such as gap junction, sodium and/or calcium channel conductances, etc.) are varied. However, the conclusions drawn when using this approach alone have been somewhat limited because of the complex and interrelated phenomena typically present in spiral waves. To overcome this difficulty, researchers have often employed simplified models of arrhythmia (e.g., pulse propagation in a ring, low dimensional maps) [2,19,26–29], and/or simplified dynamical cell models [2,3,21,30–34], or supported their studies with concepts or analytical expressions derived from these types of models [16,18,21,22,35]. The use of these simplified models has helped greatly to advance our understanding of spiral wave dynamics, but they often present some limitations. Some fail to capture mechanisms of reentry that are inherently two-dimensional in nature (e.g., dynamics of the spiral core, wavefront curvature and fundamentally two-dimensional aspects of electrotonic interaction and conduction velocity dispersion), which, as we hypothesize and some studies have already suggested [9,11,16,18,19,21,36], often play an essential role in the wave dynamics and its stability. Also, the models sometimes do not include some of the detailed electrophysiological and often interrelated processes present in spiral wave dynamics (alternans, memory, ionic mechanisms, etc.).

The application of linear perturbation theory to the system equations is another avenue taken by investigators to study spiral wave stability. This approach sidesteps some of the limitations just discussed. A nice property of this method lies in its ability to separate out various phenomena (alternans, meandering, memory, etc.) allowing one to analyze each independently and characterize stability through the use of so-

*Electronic address: nfo1@cornell.edu
URL: http://reentry.cwru.edu/otani

called "eigenmodes." The method has already been used to study the stability of a steady rotating spiral wave in two dimensions (2D) or a vortex in three dimensions (3D) [37–41]. Its implementation is, however, computationally intensive and consequently has only been applied to the FitzHugh-Nagumo (FN) equations, a relatively simple model that generally does not produce spiral wave breakup. The analysis was thus limited to a study of the meandering of spiral waves in 2D or filament twist in 3D.

The ultimate goal of studying spiral wave dynamics using these methods is to find an efficient method to prevent, suppress or control arrhythmia, and reestablish normal cardiac activity. If alternans is indeed a major player in the transition from ventricular tachycardia to ventricular fibrillation [6,12,15,18,21,27,42–44], then one step towards this goal would be to find ways to suppress or control alternans. This might be accomplished by formulating drug therapies that modify ionic currents and thereby alter the overall dynamics of the tissue. However, our lack of understanding of the complex dynamics of arrhythmia has led to catastrophic results in early drug trials (CAST and SWORD [45–47]). Electrical stimulation protocols have also been explored as an approach for the control of alternans, both at the cellular level and in 2D [48–52]. One type of protocol applied to single cells and one-dimensional (1D) cables adjusts the pacing interval to suppress alternans [51,53,54]. However, this approach seems to be difficult to extend to the case of reentry, where control cannot easily be exerted on the "pacing interval." A different approach was used by Rappel *et al.* [49]. Their control scheme applied a feedback current to a discrete set of points during repolarization, thereby controlling alternans at each point. Overdrive pacing has also been shown to control spiral wave chaos under certain conditions [55,56].

A number of methods for completely suppressing reentrant patterns using electrical stimuli have also been suggested [56–64]. These include displacing the reentrant wave towards a boundary where it will self-extinguish [58,63,64], applying suitable stimuli in the recovery phase to generate a new wavefront which would collide with and suppress the original reentrant wave [57,59,65], using pulse modulation to force the tissue to resume its normal rhythm [60], and simulating no flux boundary conditions inside the tissue using lines of stimuli, where reentry would then vanish [62,66].

Recently in our group, we have also applied linear perturbation theory to the twin goals of identifying the physiological basis for, and controlling, alternans in rapidly paced, isolated cardiac cells. A distinction relative to many of the other studies, is that we have applied the method directly to the ion channel equations. This helped us reveal the ionic process responsible for alternans [34,67] and led to the development of new, ion-channel based strategies for the electrical control of alternans in single cells [68].

Encouraged by these results, we now propose to again apply the eigenmode method at the ion channel level, this time in two spatial dimensions, to gain new insights into spiral wave dynamics, and in particular alternans, and to present a new approach for controlling spiral wave breakup. In this study, we used the three variable Fenton-Karma model (referred to as the three variable simplified ionic model or 3V-SIM) [21,22] as a first step towards the use of more detailed ionic models.

Our approach offers several advantages and improvements over other previously described studies: (1) The method is able to isolate, analyze independently and characterize the stability of the multiple and intricate phenomena involved in spiral wave dynamics, especially close to the spiral tip, where meandering is often combined with alternans. (2) In contrast to the FitzHugh-Nagumo model, the use of 3V-SIM includes the three basic ionic currents, which will allow the study of alternans and provide a basis for forming simple, but physiological, explanations of processes involved in spiral wave instability. (3) Since the method is applied to study stability in 2D rather than pulse propagation in 1D or constant pacing in a single cell, we will be able to look at mechanisms of reentry that are inherently two-dimensional. (4) The method automatically provides stimulus sensitivity information through the examination of left eigenvectors. This allows objective determination of the optimal locations and timing ofthe control stimuli for maximum efficiency. (5) The method's ability to embrace the global dynamics of the spiral wave and directly investigate the precise electrophysiological mechanisms of its instability will help in the design of smart and efficient protocols to target and control specific modes, a difficult task if phenomenological concepts such as those based on low dimensional maps and variable sets are used. These advantages must be balanced against inherent limitations of the method, which will be discussed in detail in the discussion section.

The purpose of this paper is therefore several fold: (1) To introduce the method, (2) to extract and describe spiral wave alternans mechanisms for a simple ion channel model, (3) to present a new approach for the control of alternans using knowledge obtained from perturbation theory, and (4) to demonstrate the potential of the method to develop control strategies for spiral wave instabilities. We first present linear perturbation theory as it applies to our problem, and describe how the method is implemented numerically. We then exhibit the various modes obtained, in particular the alternans modes, and describe briefly their characteristics. Finally, we demonstrate how perturbation theory can help design an efficient stimulus which, despite being very localized, can control meandering and alternans over the entire tissue, thus inhibiting breakup of the spiral wave in the nonlinear regime.

II. STUDY OF SPIRAL WAVE STABILITY

We will study the propensity for rotating action potential waves to break up by assuming that the breakup phenomenon is related to the instability of a steadily rotating action potential wave. That is, if a test were conducted in which a rigidly rotating wave is initiated in cardiac tissue, and this wave were unstable to small perturbations, leading to a progressively more and more unsteady rotating pattern and breakup, then we would expect that, more generally, arbitrary rotating wave patterns in the same medium would also be susceptible to breakup. With this assumption, we confine our study to the consideration of the stability of a single, rigidly rotating wave.

A. The method

1. The dynamical system

The system we will use will be two-dimensional and circular in geometry. The idea will be to first calculate a

steadily rotating wave solution in this system, with the center of rotation coinciding with the center of the system, and then study the stability of these solutions using linear perturbation theory.

The dynamics of this circular system will be governed by the equations of the three-variable Fenton-Karma model (3V-SIM) [22]:

$$\partial_t \boldsymbol{u} = \boldsymbol{D} \cdot (\nabla^2 \boldsymbol{u}) + \boldsymbol{\mathcal{F}}(\boldsymbol{u}) \tag{1}$$

where $\boldsymbol{u}(x,y,t)$ is the vector $[u(x,y,t),v(x,y,t),w(x,y,t)]^T$ which includes the membrane potential u, inactivation gate v of the fast inward current (sodium current) and inactivation gate w of the slow inward current (calcium current), respectively. Here the T superscript designates the transpose. $\boldsymbol{D}$ is equal to:

$$\boldsymbol{D} = \begin{bmatrix} D & 0 & 0 \\ 0 & 0 & 0 \\ 0 & 0 & 0 \end{bmatrix} \tag{2}$$

where D is the diffusion tensor as determined by the gap junction conductivities between cells, and $\boldsymbol{\mathcal{F}}$ is the vector function $[\mathcal{F}_u,\mathcal{F}_v,\mathcal{F}_w]^T$, the component functions which define the local (i.e., isolated) cell behaviors for u, v, and w, respectively, as described in Appendix A.

This model was chosen mainly for its simplicity due to the intensive computing involved with our method, and for its ability to produce spiral wave breakup. Despite its simplicity, the model has been shown to accurately reproduce key aspects of the dynamics of other more detailed and advanced ionic models such as the Beeler-Reuter, Luo-Rudy-I or Courtemanche *et al.* models [21,22] with appropriately chosen parameters.

The 3V-SIM parameters were chosen to reduce the rate of rise of the upstroke to about 30 V/s compared to the normal value of about 200 V/s, assuming an AP amplitude of 100 mV. This was accomplished by reducing the fast inward conductance g_{fi} while simultaneously decreasing the gap junction resistance to keep the propagation velocity similar to that of healthy tissue. (See Appendix A for parameter values and definitions.) This was done for two reasons. First, we were principally interested in studying alternans as a cause of spiral breakup; thus the parameters were chosen to limit the meandering instabilities relative to instabilities associated with alternans. Second, it was necessary to have "smoother" functions to facilitate the convergence of the Newton-Raphson method, which was used to find the steady state (as described later in this section). To ensure proper convergence, we also modified the model's equations to make them second order differentiable. The new set of equations is described in Appendix A.

Computer simulations of spiral waves were performed to verify the appropriateness of our choice of system parameters. Simulations were conducted in polar geometry with a system radius of 3 cm. We used 100 computational nodes in the radial direction and 600 in the azimuthal direction.

The integration of the equations forwards in time was performed using the standard forward Euler (FE) method for the local dynamics terms and any terms involving radial derivatives. The Crank Nicholson method was employed for any terms involving azimuthal derivatives to avoid the stringent stability timestep limit imposed on the FE (on the order of 10^{-4} ms) arising from the very small azimuthal grid spacing at the very center of the polar grid. Solution to the equations was then facilitated by using a standard FFT with respect to the azimuthal coordinate, θ. The parameter values of the 3V-SIM model were those listed in Appendix A. The timestep was generally chosen to be 0.01 ms. (This is much smaller than the fastest timescale which is approximately equal to $\tau_d \approx 0.3-0.6$ ms; see Appendix A for definition.)

2. Linear perturbation theory

When a rigidly rotating wave is unstable, linear perturbations (i.e., small changes in membrane voltage or the other dynamical quantities) will typically grow, often leading to spiral wave breakup in the nonlinear (i.e., large-amplitude) regime. When small, these perturbations can be regarded as the sum of a number of independent components, called eigenmodes, each of which is associated with a distinct type of behavior, such as spiral wave meandering or alternans. Eigenmode theory, which is derived from linear perturbation theory, allows the extraction and study of the growth and nature of each of those modes independently.

The first step of the method consists of finding a rigidly rotating spiral wave solution to the governing equations, which we refer to as the "steady state." Mathematically, this can be achieved by looking for a nontrivial steady state solution to Eq. (1) in the frame of reference rotating at the same angular frequency Ω as the spiral wave. The natural coordinate system to use with this method for our system is polar coordinates (r,θ) where r is the radius distance from the center of rotation and θ the azimuthal angle. Transformation to the rotating frame consists of making the following change of variables: $r \rightarrow r$, $\theta \rightarrow \theta - \Omega t$ and $t \rightarrow t$. This transformation results in the addition of an advection term of the form $\Omega \partial_\theta \boldsymbol{u}$ to Eq. (1); that is,

$$\partial_t \boldsymbol{u} = \boldsymbol{\mathcal{G}}(\boldsymbol{u}) \tag{3}$$

where

$$\boldsymbol{\mathcal{G}}(\boldsymbol{u}) \equiv \Omega \partial_\theta \boldsymbol{u} + \boldsymbol{D} \cdot (\nabla^2 \boldsymbol{u}) + \boldsymbol{\mathcal{F}}(\boldsymbol{u}). \tag{4}$$

A rigidly rotating wave is stationary in this frame, implying that the time derivatives must be zero. The steady state solution $\boldsymbol{u}_0(r,\theta)$ must, therefore, satisfy:

$$\boldsymbol{\mathcal{G}}(\boldsymbol{u}_0) = 0. \tag{5}$$

Once the steady state is obtained, we can determine the dynamics governing small perturbations $\boldsymbol{\delta u}$ around the steady state by expanding Eq. (3) to first-order:

$$\partial_t \boldsymbol{\delta u} = \boldsymbol{\mathcal{D}}(\boldsymbol{\mathcal{G}}(\boldsymbol{u}_0))\,\boldsymbol{\delta u} \tag{6}$$

where $\mathcal{D}$ is the Jacobian with respect to u, v, and w. In other words:

$$\mathcal{D}(\mathcal{G}(\boldsymbol{u}_0)) = \Omega\partial_\theta + \boldsymbol{D}\nabla^2 + \begin{pmatrix} \partial_u\mathcal{F}_u(\boldsymbol{u}_0) & \partial_v\mathcal{F}_u(\boldsymbol{u}_0) & \partial_w\mathcal{F}_u(\boldsymbol{u}_0) \\ \partial_u\mathcal{F}_v(\boldsymbol{u}_0) & \partial_v\mathcal{F}_v(\boldsymbol{u}_0) & 0 \\ \partial_u\mathcal{F}_w(\boldsymbol{u}_0) & 0 & \partial_w\mathcal{F}_w(\boldsymbol{u}_0) \end{pmatrix}. \quad (7)$$

We study the dynamics of the perturbations $\boldsymbol{\delta u}$ as expressed in Eq. (6) by finding the eigenmodes of the system. Each eigenmode $\boldsymbol{a}(r,\theta)$ and its eigenvalue λ satisfy the dynamical equation:

$$\mathcal{D}(\mathcal{G}(\boldsymbol{u}_0))\boldsymbol{a} = \lambda\boldsymbol{a} \quad (8)$$

so that, if the initial perturbation $\boldsymbol{\delta u}$ has the form, $\boldsymbol{\delta u}(r,\theta,0)=\boldsymbol{a}(r,\theta)$, then $\boldsymbol{\delta u}$ satisfying Eq. (6) is forever proportional to the eigenmode:

$$\boldsymbol{\delta u}(r,\theta,t) = \boldsymbol{a}(r,\theta)e^{\lambda t}. \quad (9)$$

Each mode is, therefore, characterized by its eigenvector and eigenvalue. The eigenvector gives the spatial structure of the perturbation for the membrane potential and the other variables as we shall see in Sec. II B. The eigenvalue is a complex number containing the growth rate and frequency of the mode. As suggested by Eq. (9), the real part of the eigenvalue ($\equiv\lambda_R$) is the growth rate, indicating how fast the perturbation associated with the mode grows (positive value) or decays (negative value). The imaginary part of the eigenvalue (λ_I) is the mode frequency, which gives the oscillation frequency of the mode. For instance, the alternans modes have mode frequencies very close to half the spiral wave rotation frequency, which implies that the width oscillation completes half of its cycle during each period of rotation. This is consistent with alternans as classically defined, in which the action potential duration alternates from beat to beat.

3. The numerical method

To solve Eq. (5) for the steady state and Eq. (8) for the eigenmodes, we use to a large extent the numerical approach presented by Henry and Hakim [40,41], which will be briefly described here. More details can be found in Appendix B. The MATLAB software package (Mathworks, Inc.) is used to perform all computations.

The steady state is found using the Newton-Raphson method applied to the discretized version of Eq. (5). We first find the steady state of a stable spiral wave having a circular core obtained with a reduced value for the conductance associated with the fast inward (sodium) current ($g_{fi}=1.4$ mS/cm^2) compared to the "standard" case. Once the steady state is found for a stably rotating wave, g_{fi} was stepwise increased with the new steady state being calculated at each step. The steady state obtained for the previous value of g_{fi} was used as the initial guess in the Newton-Raphson algorithm for each new value of g_{fi}. This procedure was performed up to sodium conductance values for which the spiral wave breaks up.

Once the steady states are found, we extract the dominant perturbation eigenmodes of the discretized version of Eq (7). This is accomplished by extracting an approximation to the subspace spanned by, say, the 100 most dominant eigenmodes with the 100 largest growth rates using a modified version of the Arnoldi method [69]. Once this subspace is obtained, we can easily extract an approximation to the 100 dominant eigenvalues and corresponding eigenvectors. Those modes are defined as the right eigenmodes of the system in contrast to the left eigenmodes which will be defined in Sec. III A.

Discretization is accomplished through the use of a polar grid composed of $N_r=100$ grid points in the radial direction and $N_\theta=606$ points in the azimuthal direction, with a single extra grid point in the center of the grid. We define $N=1+N_rN_\theta$, the total number of grid points, and $\boldsymbol{u}\equiv[u^1,u^2,\ldots,u^N,v^1\ldots,v^N,w^1,\ldots,w^N]^T$, where u^i, v^i, and w^i correspond to the variables u, v and w associated with the ith cell on the polar grid, totaling $3N=3+3\times100\times606\approx180\,000$ variables. When there is no ambiguity, we have found it convenient to use the same notation $\boldsymbol{u}$ for both the spatially discrete and continuous vector representation of the state variables. The grid spacings in the radial and azimuthal directions were chosen to be $\Delta r=0.03$ cm and $\Delta\theta=2\pi/606$, resulting in a disk-shaped patch of radius 3 cm. The grid spacings are thus substantially smaller than the resting space constant, $\sqrt{D/g}\approx1$ mm, as required for numerical accuracy. (Here g is the total ion channel conductance at rest.)

B. Results

The appropriateness of our choice of parameters for the 3V-SIM was verified by running several simulations of spiral waves and their breakup for different values of g_{fi} using the numerical method described in the Methods section. A typical spiral wave and its breakup is shown in Fig. 1 for $g_{fi}=1.75$ mS/cm^2. To study breakup, we perturbed a steady state spiral wave by adding spatially random noise (of 0.001 amplitude) at time $t=0$ to the membrane voltage component. This noise was introduced to hasten the onset of breakup which would have appeared anyway, due to the presence of small amplitude perturbations resulting from numerical and roundoff errors, but only after a much longer period of time. Note that, as intended, the spiral wave does not noticeably meander, and that breakup occurs due to increasing oscillations in the spiral width, consistent with spiral wave alternans. The spiral almost breaks up at 225 ms before going through another alternans cycle to eventually break at around 450 ms.

When linear perturbation theory was applied to the particular simulation case described above for a fast inward conductance of $g_{fi}=1.75$ mS/cm^2, we found a number of modes of interest among the 100 largest eigenmodes (i.e., those with the largest growth rates). We found the usual translational (eigenvalues close to $\pm i\Omega$) and rotational modes (zero eigenvalue) which do not reveal any important dynamics of the perturbations. These modes are a reflection of the fact that the rotated and translated versions of the steady state are themselves steady states. We also found one dominant meandering mode, which has been studied extensively in previous publications [37,39,40]. Apart from these well-known modes, we found not just one but several alternans modes

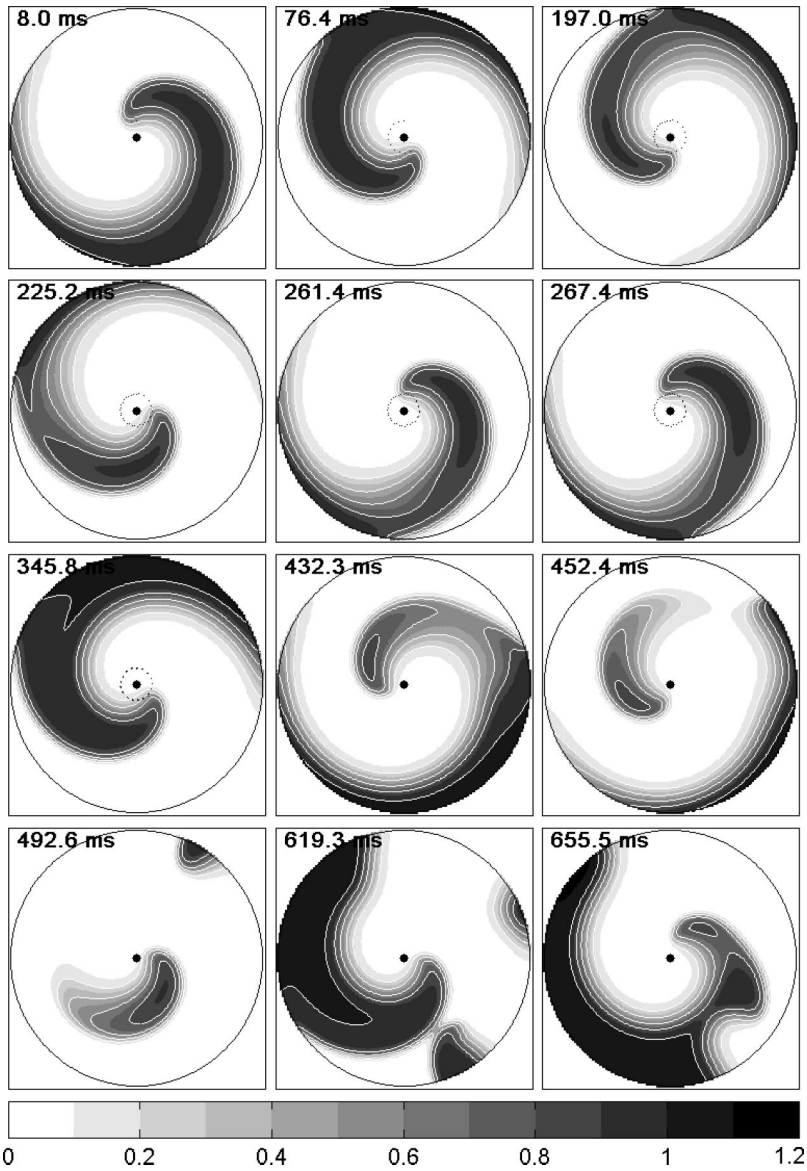

FIG. 1. Membrane potential u and its contours (white solid line) at different times showing spiral wave breakup for the case where $g_{fi} = 1.75\ \mathrm{mS/cm^2}$. The time related to each frame is shown in the top left corner. The rotation period is 131 ms. Increasing alternans amplitude in the spiral width leads eventually to breakup at time close to 430 ms. Meandering does not occur, as evidenced by the circular trajectory of the spiral tip (black dotted line). The movie related to this figure can also be found in Ref. [70].

having different degrees of instability and different mode frequencies. The eigenvalues associated with the 21 largest eigenmodes are shown in Fig. 2. Note that the alternans modes frequencies are approximate half integer multiples of the rotation frequency Ω (i.e., $\pm\Omega/2$, $\pm 3\Omega/2$, $\pm 5\Omega/2$, etc.) This is consistent with the frequency of the modes found for perturbations of action potentials traveling around a ring [27]. It is also consistent with the alternans nature of these modes—in alternans, the pattern repeats every two pacing periods at every point in the lab frame, and repeats with opposite sign every period. Since any point in the rotating frame returns to the same point after each rotation of the wave, the pattern as observed in the rotating frame will also repeat every two rotations, and have opposite polarity each rotation. Consequently, the real part of the frequency of these modes can only be half-integer multiples of the wave rotation frequency.

For simplicity and comparative purposes, we will describe in detail three typical alternans modes chosen for their differences in frequency, spatial structure and/or behavior. The eigenvalues of these modes are labeled in Fig. 2. The fastest growing mode, which we will refer to as Alternans Mode 1, is the one we would normally expect to be the main cause for breakup in the nonlinear regime. It also has the lowest mode frequency, being equal to $\Omega/2$. Other modes of interest will be referred to as Alternans Modes 2 and 3. These three eigenmodes have eigenvalues $(\lambda_R, \lambda_I) = (1.14\Omega/2\pi, 0.5\Omega)$, $(0.38\Omega/2\pi, 3.5\Omega)$, and $(-0.39\Omega/2\pi, 0.5\Omega)$, respectively.

Although the frequency of a mode can give us a clue as to the type of mode it is, alternans modes can only be rigourously differentiated from other modes, including the meandering mode, by looking at their spatial structures. Figure 3 shows a typical time course for an alternans mode perturbation (Alternans Mode 1), showing its various phases through one mode period. We plotted the sum of membrane potential components, $\boldsymbol{a}e^{\lambda_I t}$ and $\overline{\boldsymbol{a}}e^{\overline{\lambda}_I t}$ of a related pair of alternans eigenmodes having complex conjugate eigenvalues $\lambda = (\lambda_R, \pm\lambda_I)$. (Here the overbar designates complex conjugation.) The perturbation amplitude and width increase as the perturbation propagates along the spiral wave leading and

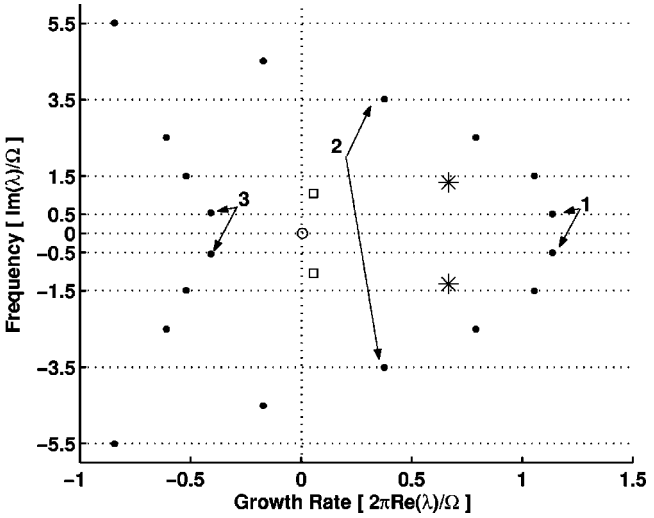

FIG. 2. Eigenmode map showing the eigenvalues λ_m corresponding to the most unstable modes for $g_{fi}=1.75$ mS/cm^2. The frequency of each mode (imaginary part of λ) normalized to Ω is plotted versus its growth rate (real part of λ) normalized to $\Omega/2\pi$. The rotational, translational and meandering modes are represented by circle, square and star symbols respectively. All the other dominant modes, represented by points, are alternans modes. The eigenvalues of the eigenmodes are arranged in complex conjugate pairs, of which five (excluding the rotational and translational modes) are unstable with positive growth rates. Note that the frequencies of the alternans modes are near half-integer multiples of Ω. The pairs of eigenvalues designated as 1, 2, and 3 refer to Alternans Modes 1, 2, and 3, as discussed in the text.

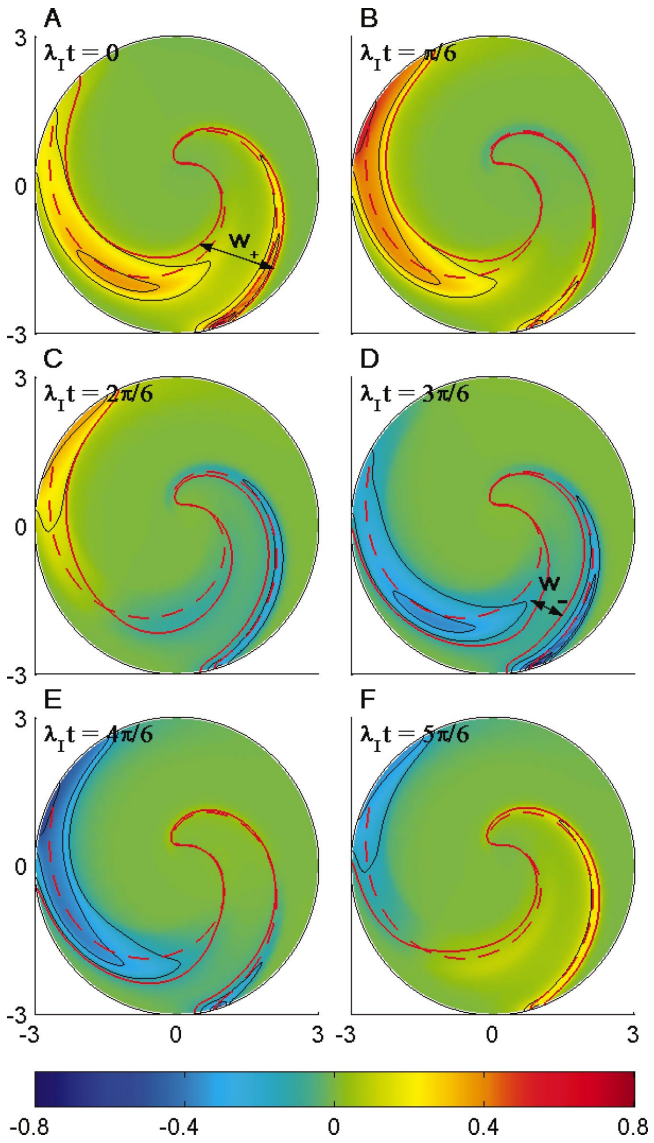

FIG. 3. (Color) Snapshots of the membrane potential perturbation associated with an alternans eigenmode, and its effect on the spiral wave. The mode frequency is $\Omega/2$. The snapshots were taken $1/6^{th}$ of an eigenmode period apart. The contour of the spiral wave is shown as a red dashed line for the steady state and as a solid line after the perturbation has been added. For the purpose of illustration, the red line contours were drawn using an artificially large perturbation amplitude (3 times that of the normalized eigenmode). A positive perturbation (yellow-red) leads to a widening while a negative perturbation (blue) to a narrowing of the spiral wave width. The width fluctuates between w_+ and w_-, typical of alternans. The depolarized region of the spiral wave may be distinguished from the recovery region because it is always narrower, for the parameters we use in this study (as illustrated explicitly in Fig. 1). The movie related to this figure can also be found in Ref. [70].

trailing edges outward from the point of zero curvature near the spiral wave tip. The sign of the perturbation is the same on both sides of the steady state spiral wave (shown in red when positive and blue when negative), which translates into a widening or narrowing of the perturbed spiral wave width, as shown by the solid red line contour. The spiral width is seen to vary between the widths w_+ and w_- shown in panels A and D. These alternations in the action potential width, together with the fact that they occur over a period of two rotation periods, is strongly indicative of alternans.

The oscillation pattern of any perturbation mode $\boldsymbol{a}_m$, as shown in Fig. 3 for the dominant mode, can be succinctly represented by plotting its amplitude $|\boldsymbol{a}_m|$ and phase $\phi(\boldsymbol{a}_m)$. This representation was used to show the spatial structure of the membrane potential component of the perturbation for Alternans Modes 1, 2, and 3 and the meandering mode in Fig. 4.

Note that, for all alternans modes, the red isophase contours run perpendicular to the spiral wave edges, indicating that the perturbations on the two edges are in phase, which is typical of alternans. In contrast, for the meandering mode, the perturbations on the two edges are 180° out of phase, as shown in panel H. This corresponds to local translational shifts of the spiral wave relative to its steady state counterpart, with no significant increase or decrease of the wave width. We observe this translational motion to be generally circular as a function of time in the rotating frame. Since the mode frequency λ_I (here $\approx 1.3\ \Omega$) is not commensurate with the wave rotation frequency Ω, the result in the lab frame is a combination of the circular translational motion with the overall rotation of the spiral wave. This creates the flower petal like motion of the wave characteristic of spiral wave meandering. For Alternans Modes 1 and 3, the phases of the perturbations change rather modestly along the entire length

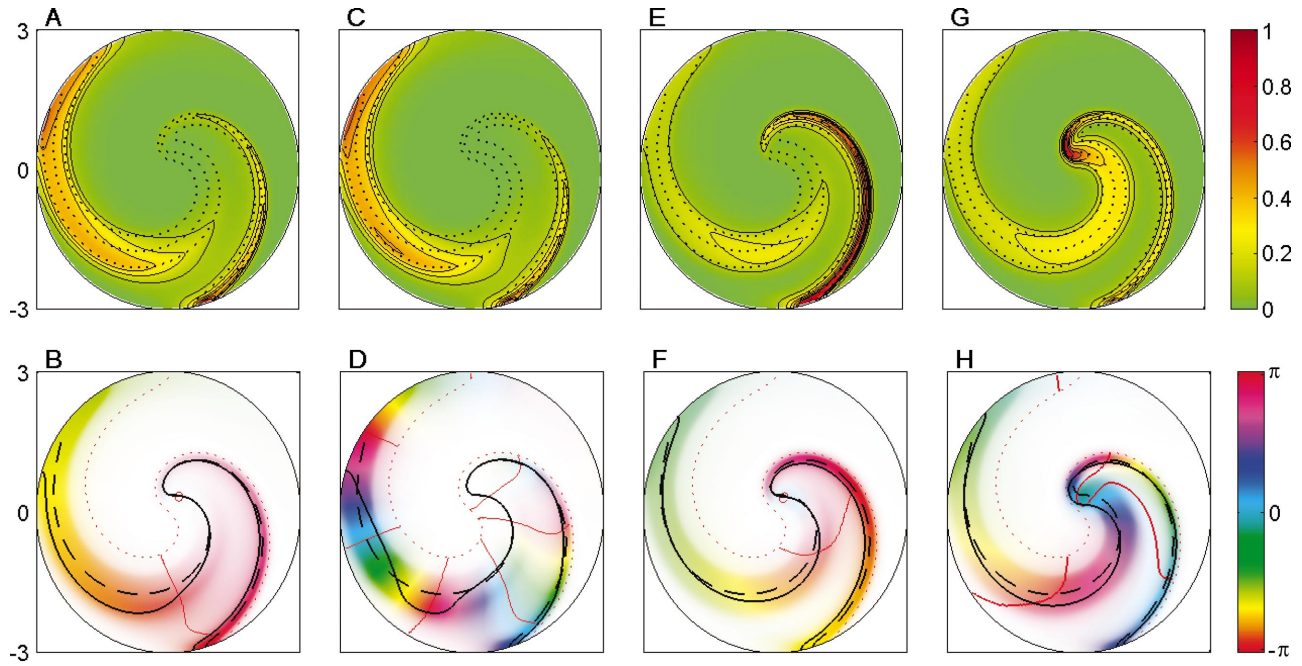

FIG. 4. (Color) Amplitude (top panels) and phase (bottom panels) plots for the Alternans Mode 1 $(\lambda_R,\lambda_I)=(0.14\Omega/2\pi,0.5\Omega)$ in panels A and B, Alternans Mode 2 $(0.38\Omega/2\pi,3.5\Omega)$ in panels C and D, Alternans Mode 3 $(-0.39\Omega/2\pi,0.5\Omega)$ in panels E and F, and the meandering mode $(0.68\Omega/2\pi,1.33\Omega)$ in panels G and H. In the amplitude plots, mode amplitudes are represented by the various colors appearing in the colorscale to the right, while steady state membrane potential level contours, shown as black dotted lines, reveal the location of the steadily rotating spiral wave. In the phase plots, the intensity of the color associated with the phases is proportional to the amplitude, while the color itself represents the mode phase. Outlines of both the steady state and perturbed spiral waves are shown as black dashed and solid lines, respectively, in the phase plots. For the purpose of illustration, the black line contours were drawn using an artificially large perturbation amplitude (3 times that of the normalized eigenmode). The red solid line contours in the phase plot are isophase contours plotted every π radians. For clarity, these contours are only plotted in and around the depolarized region of the steady state. Movies showing the phase patterns and amplitude of each mode in a similar manner as in Fig. 3 can also be found in Ref. [70].

of both leading and trailing edges of the spiral wave. On the other hand, for higher frequency modes, such as Alternans Mode 2, the perturbation phase rotates through several multiples of 2π (6π for Mode 3) as one travels outward along either wave edge. This produces rapid spatial oscillations of the spiral wave width, as exhibited by the solid black line perturbed wave outline in panel D for Mode 3. This is typical of discordant alternans (i.e., alternans that exhibit opposite polarities in different regions of the tissue [71]). Differences other than just the mode frequencies exist among the various alternans modes. Some seem to display larger perturbations near the spiral tip than others, while in some cases, there are greater perturbations in the wake of the spiral wave than on the wavefront. These differences seem to present themselves more distinctly when comparison was made between modes belonging to different parabola-shaped sets of points in Fig. 2, rather than among modes of the same set. For instance, such differences appear when comparing Alternans Mode 3 with either Alternans Mode 1 or Mode 2 in the top panels of Fig. 4. Perturbations associated with Alternans Mode 3 also seemed to involve the tip of the spiral wave more than those of Alternans Modes 1 and 2. These variations in the spatial structure of the various modes suggest the existence of physiologically different types of alternans [18,21], for which further analysis is needed.

It is well known that the dynamics and, in particular, the propensity for breakup of the spiral wave are highly dependent on the parameter values of the ionic model. As an example, to illustrate the dependency of the eigenmodes on the 3V-SIM parameter values, we computed the eigenmodes and their eigenvalues for various values of the fast inward current conductance (g_{fi}). The results are shown in Fig. 5, where the translational, rotational, meandering and dominant alternans eigenmode eigenvalues are plotted for different values of g_{fi}. The trajectories of the eigenvalues are represented by solid lines as g_{fi} is increased from 1.5 to 3.5 $\mathrm{mS/cm^2}$. As the conductance of the fast inward current (g_{fi}) is increased, so do the growth rates of all the alternans and meandering modes. (The translational and rotational growth rates do not increase—they are theoretically independent of g_{fi}.) The alternans mode frequencies remain relatively unchanged relative to Ω. (The rotational frequency Ω does increase, however, as g_{fi} increases.) The meandering mode seems to drift toward higher frequencies. The increased instability of the alternans and meandering modes with g_{fi} is consistent with the spiral wave's greater tendency to break up and meander at high conductance of the fast inward current (sodium current) as seen in the simulations and as previously observed by others [17,18,35]. Finally, we note that the relative positions of the alternans mode eigenvalues change at high g_{fi} (as illustrated by the dotted line) leading to the emergence of a dominant mode with frequency higher than $\Omega/2$.

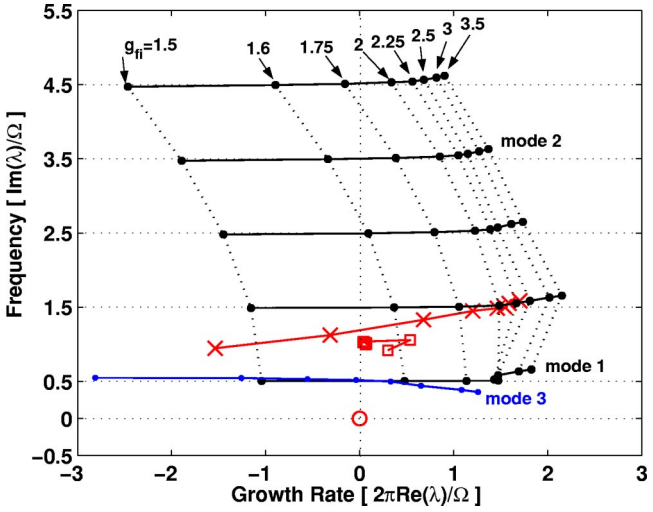

FIG. 5. (Color online) Eigenmode map showing the dominant eigenvalue λ for each (approximate) half-integer mode frequency for several values of g_{fi} (1.5, 1.6, 1.75, 2, 2.5, 3, and 3.5 mS/cm^2). Only positive half-integer frequency eigenvalues are shown for simplicity. (The negative frequency eigenvalues are a mirror-image.) The mode frequencies $(\mathrm{Im}(\lambda)/\Omega)$ are plotted versus the mode growth rate $(2\pi\,\mathrm{Re}(\lambda)/\Omega)$. The eigenvalues associated with the rotational, translational, meandering and alternans modes are shown as circles, squares, crosses, and points, respectively. A black line is drawn through the dominant alternans modes of each half-integer frequency. Additionally, a blue line (smaller dots) is drawn through the next lower dominant mode for the $\Omega/2$ frequency alternans mode (corresponding to the Alternans Mode 3). The red line with crosses shows the motion of the meandering eigenvalues, while the red line with squares indicates the behavior of thetranslational eigenvalue. Note that, for larger conductances g_{fi}, the $3\Omega/2$ frequency eigenvalue takes over from the $\Omega/2$ eigenvalue as the eigenvalue for the fastest growing mode.

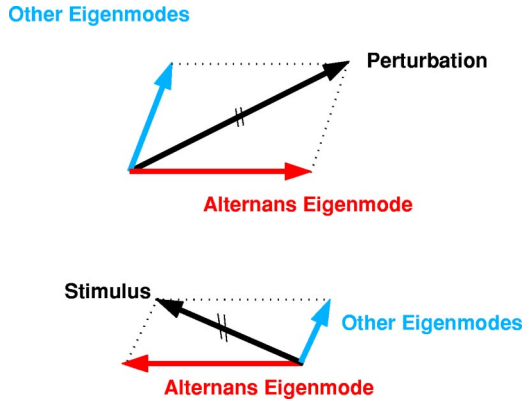

FIG. 6. (Color online) Any modes (black arrows) can be decomposed into components along the alternans mode to be suppressed (red vectors) and other modes (blue vectors). In order to suppress the undesired alternans mode, the stimulus amplitude (lower black arrow) must be adjusted so that its alternans component (vector in red) is exactly equal and opposite of that (red) of the perturbation (top black arrow).

III. CONTROL OF ALTERNANS

We can use knowledge gained through the eigenmode analysis of spiral wave stability to develop methods for preventing spiral wave breakup. The goal here is to cancel or stabilize the unstable eigenmode components of perturbations present in the rotating wave. To achieve this goal, we first show how left eigenvectors can be used to design a stimulus protocol to cancel any unstable mode. We then show an example in which alternans can be controlled with the application of a single, properly chosen stimulus.

A. Method

In the linear regime, any arbitrary perturbation may be expressed as a linear combination of the eigenvectors, each of which grows or decays exponentially with its own rate constant, λ_m. Thus, for a given perturbation $\boldsymbol{\delta u}$, we can write:

$$\boldsymbol{\delta u}(t) = \sum_{m=1}^{3N} \delta u_m \boldsymbol{a}_m e^{\lambda_m t} \tag{10}$$

where the δu_m's are constants.

We can eliminate the mth mode component of the perturbation by applying a current pulse I^i to the ith cell, associated to the ith variable, at some time t_0. If the pulse duration Δt is much shorter than the fastest time scale of the membrane dynamics, the cell membrane potential will be increased or decreased by a voltage offset $\Delta V^i = I^i \Delta t/(S^i c)$, where c is the membrane capacitance per unit area. This voltage offset may also be thought of as an added perturbation to the system, so that it too can be represented in terms of eigenmodes:

$$[0,0,\ldots,0,\Delta V^i,0,\ldots,0]^T = \sum_{m=1}^{3N} s_m \boldsymbol{a}_m \tag{11}$$

where the s_m's are constants.

We can think of this situation schematically as shown in Fig. 6 where both the preexisting perturbation and the stimulus can be decomposed into the mth mode (an unstable alternans mode, in red) and all their other component eigenmodes, grouped together in one vector (in blue). If the amplitude of the stimulus is chosen so that its mth eigenmode component is equal and opposite in amplitude to the mth component, the alternans component we wish to eliminate, as suggested by the length and direction of the red arrows in Fig. 6, it is clear that this alternans mode will immediately be suppressed when the stimulus is applied, effectively eliminating the corresponding instability. Comparing Eq. (10) at time t_0 to Eq. (11), we see that, mathematically, the stimulus amplitude should be chosen so that, $s_m = -\delta u_m e^{\lambda_m t_0}$.

The required stimulus amplitude can be calculated rigourously by using the left eigenvectors of the system, which are defined in relation to the inner product in polar coordinates, $\langle , \rangle$ given as,

$$\langle \boldsymbol{z}_1, \boldsymbol{z}_2 \rangle \equiv \sum_{i=1}^{3N} \overline{z_1^i} z_2^i S^i \tag{12}$$

for any two vectors $\boldsymbol{z}_1$ and $\boldsymbol{z}_2$.

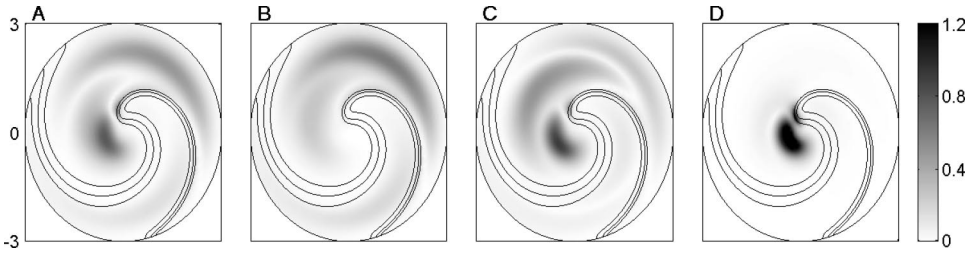

FIG. 7. Amplitudes of the left eigenvectors corresponding to Alternans Modes 1, 2, and 3 (panels A, B, and C) and the meandering mode (panel D). Level membrane potential curves of the steady state are shown as contours.

Any left eigenvector $\tilde{\boldsymbol{a}}_m$ has the nice property of being perpendicular to all the right eigenvectors of the system except its associated right eigenvector $\boldsymbol{a}_m$; i.e., $\langle \tilde{\boldsymbol{a}}_n, \boldsymbol{a}_m \rangle = 0$ for $n \neq m$ (see Appendix C for more details). We can, therefore, calculate both coefficients δu_m and s_m by taking the inner product of $\boldsymbol{\delta u}(t_0)$ and $[0,0,\ldots,0,\Delta V^i,0,\ldots,0]^T$ with $\tilde{\boldsymbol{a}}_m$ in Eqs. (10) and (11). We then obtain:

$$s_m = \frac{\langle \tilde{\boldsymbol{a}}_m, [0,0,\cdots,0,\Delta V^i,0,\cdots,0]^T \rangle}{\langle \tilde{\boldsymbol{a}}_m, \boldsymbol{a}_m \rangle} = \frac{\overline{\tilde{a}_m^i} \Delta V^i S^i}{\langle \tilde{\boldsymbol{a}}_m, \boldsymbol{a}_m \rangle} \tag{13}$$

and

$$-\delta u_m e^{\lambda_m t_0} = -\frac{\langle \tilde{\boldsymbol{a}}_m, \boldsymbol{\delta u}(t_0) \rangle}{\langle \tilde{\boldsymbol{a}}_m, \boldsymbol{a}_m \rangle} \tag{14}$$

which, by setting $s_m = -\delta u_m e^{\lambda_m t_0}$ yields,

$$\Delta V^i S^i \overline{\tilde{a}_m^i} = -\langle \tilde{\boldsymbol{a}}_m, \boldsymbol{\delta u}(t_0) \rangle \tag{15}$$

which may also be expressed as,

$$I^i \Delta t = -\frac{c \langle \tilde{\boldsymbol{a}}_m, \boldsymbol{\delta u}(0) \rangle}{\overline{\tilde{a}_m^i}} e^{\lambda_m t_0} \tag{16}$$

showing the explicit dependence of the required charge $I^i \Delta t$ on t_0. Since the charge must be real, Eq. (16) imposes a condition on the timing (associated with the phase) as well as the amount of charge. Specifically, for a positive charge, we require that,

$$t_0 = \frac{\pi - \phi(\tilde{a}_m^i) - \phi(\langle \tilde{\boldsymbol{a}}_m, \boldsymbol{\delta u}(0) \rangle)}{\mathrm{Im}(\lambda_m)} \tag{17}$$

and

$$I^i \Delta t = c \left| \frac{\langle \tilde{\boldsymbol{a}}_m, \boldsymbol{\delta u} \rangle}{\tilde{a}_m^i} \right| e^{\mathrm{Re}(\lambda_m) t_0} \tag{18}$$

where $\phi(x)$, $|x|$, $\mathrm{Re}(x)$ and $\mathrm{Im}(x)$ stand for the angle, amplitude, real part and imaginary part of the complex number x. Analogous expressions hold for a negative stimulus charge. Note that the $\mathcal{L}_2$ norm used to normalized the eigenvectors (cf. Appendix B) and, therefore, the product $\langle \tilde{\boldsymbol{a}}_m, \boldsymbol{\delta u} \rangle$ is independent of the choice of grid spacing or type of grid used to first approximation, since the inner product is weighted by the grid point area (see definition earlier). Consequently, given the expression of Eq. (18), the amount of charge required to suppress a particular mode is independent of the grid cell area and, therefore, the choice of the level of discretization. On the other hand, the membrane potential offset ΔV^i necessary to suppress the mode does change with the grid cell area in which the stimulus is applied. It will be larger for smaller cells since $\Delta V^i = I^i \Delta t / (S^i c)$.

The presence of $\tilde{a}_m^i$ in the denominator of Eq. (18) means that the amplitude of the left eigenvector as a function of space can be considered to be a measure of the sensitivity of the mth eigenmode to modification when a stimulus is applied to the ith cell. Since the choice of an energy efficient stimulus is important while suppressing a particular mode, we should generally attempt to apply the stimulus where the amplitude of the left eigenvector is the largest (and therefore the amount of charge required is the smallest).

Note finally that the charge $I^i \Delta t$ and timing t_0 that cancel a certain eigenmode also eliminate the corresponding complex conjugate eigenmode. This can be easily seen by taking the complex conjugate of Eq. (15). Since both the perturbation, $\boldsymbol{\delta u}(t_0)$, and the voltage offset resulting from stimulation, ΔV^i, must be real, this yields exactly the relationship that must be satisfied to eliminate the complex conjugate eigenmode for these same values of $\boldsymbol{\delta u}(t_0)$ and ΔV^i (and, therefore, $I^i \Delta t$ and t_0).

B. Results

When the sensitivities of Alternans Modes 1, 2, and 3 and the meandering mode, as measured by the left eigenvectors, are plotted as functions of space, we obtain the diagrams shown in Fig. 7. One can see that, in all cases, the stimulus should be applied in the recovery region (i.e., in the region outside the spiral wave), where the left eigenvector amplitudes are the largest. For Alternans Modes 1 and 3 and the meandering mode, the sensitivity to a stimulus is greatest close to the center of rotation, while for Alternans Mode 2 it is greatest some distance from the center.

We have seen that a simple stimulus applied at the proper time and with proper amplitude in a single cell can eliminate any conjugate pair eigenmodes even though these modes have significant amplitude throughout the tissue. Thus, in theory, we would, therefore, need five stimuli to eliminate all five pairs of unstable modes for the case of $g_{fi} = 1.75\ \mathrm{mS/cm^2}$. The development of an appropriate algorithm turns out to be somewhat tricky, so we settle here for a demonstration wherein a single stimulus cancels all five unstable pairs of modes in a specially chosen perturbation. To do this, we simply choose the values δu_m for all the unstable modes equal to $-s_m$ for a given stimulus strength and timing. The stimulus was applied at a single grid point where the amplitudes of the left eigenmodes associated with the five unstable modes are generally the largest—that is, close to the center of rotation. This stimulus was generated by artificially increasing or decreasing the membrane voltage of the chosen

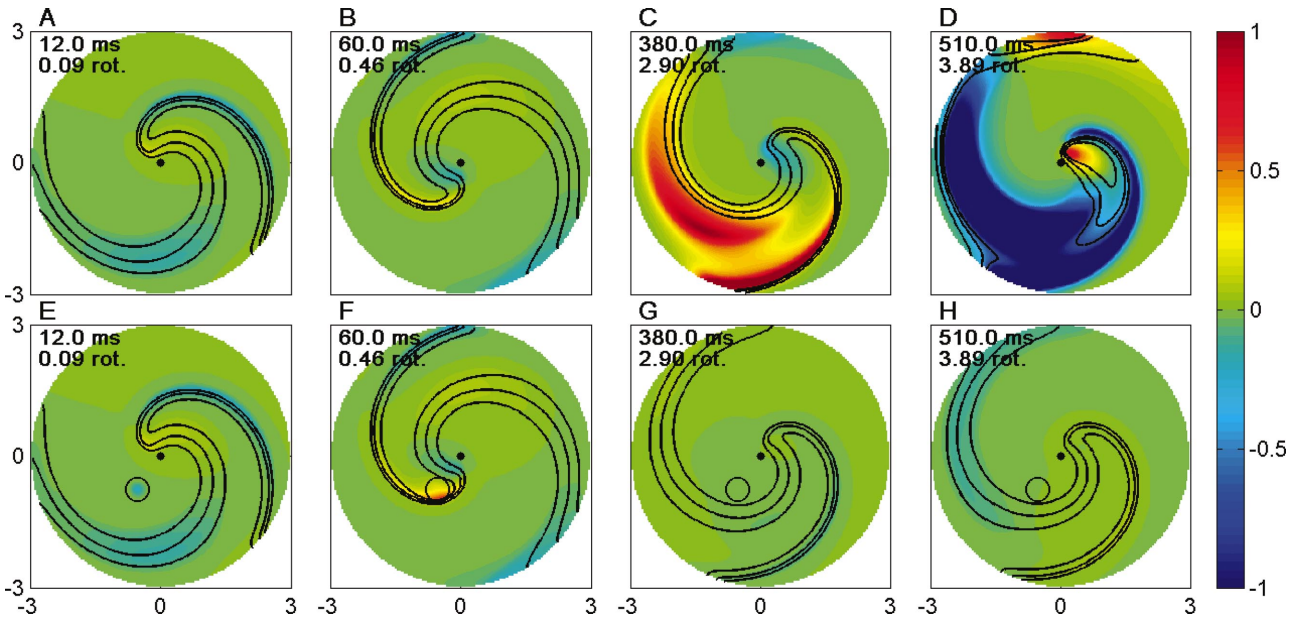

FIG. 8. (Color) Snapshots of the membrane potential perturbation in the lab frame taken at selected times (12, 60, 380, and 510 ms) for the case where no control stimulus is applied (top subplots) and for the case for which a control stimulus is introduced at time $t=10$ ms (bottom subplots). The two cases were initialized with the same, specially chosen perturbation, as described in the text. Level membrane potential contours are shown in black lines. A small black circle was drawn in each of the lower subplots to designate the region in which the stimulus was applied. The movie related to this figure can also be found in Ref. [70].

grid point, during one timestep, by the corresponding value of ΔV as defined by Eq. (15).

The results for this specially designed case are shown in Fig. 8. The specially chosen perturbation was first introduced at time $t=0$. For the controlled case, the calculated stimulus was applied at $t=10$ ms, within the small circle seen in panel E. At $t=12$ ms in panel E, evidence of the stimulus current diffusing to neighboring cells appears in the form of a blue coloration. For the uncontrolled case, the perturbation reaches amplitudes that would be large enough to produce breakup if nonlinear dynamics had been included, as suggested by the black contours in panel D. Note that we chose a large initial perturbation amplitude for the purpose of illustration (on the order of 0.2 for the membrane potential). The behavior we see for the uncontrolled case is mainly caused by the alternans mode, as suggested by the widening of the spiral wave width in panel C, one rotation period prior to the narrowing of the width in panel D. In contrast, in the controlled case, the perturbation amplitudes remain small during at least four complete rotations of the spiral wave.

The effect of the stimulus is further clarified by considering the behavior of the individual modes, as shown in Fig. 9. In this plot, the component amplitudes δu_m of selected unstable and stable modes that comprise the perturbation were calculated and plotted as functions of time. As expected, when no stimulus is applied, the stable mode amplitudes decrease while the unstable modes grow exponentially. The same is true of the controlled case, except that, when the stimulus is applied at $t=10$ ms, the unstable mode amplitudes are drastically reduced by two orders of magnitude, as clearly seen in panel B. Note that the unstable modes were not completely eliminated due to the presence of perturbations introduced by round-off and numerical errors. Nevertheless, it took 5 spiral wave rotations for the amplitudes of these modes returned to their initial values. In contrast, some of the stable mode amplitudes increased quite significantly, by two orders of magnitude when the stimulus was applied, although the resultant amplitudes were still smaller than the largest initial perturbation amplitude (about 0.2 times as large). Some of the modes exhibiting this sudden jump in amplitude were modes, which, while stable, had relatively modest damping rates.

IV. DISCUSSION

Using the linear perturbation method, we were able to extract the various modes and in particular alternans modes involved in the spiral wave dynamics. We find that, due to the 2D nature of spiral waves, the alternans modes have additional features compared to alternans in the single cell, which are characterized principally by a long-short-long-short alternation in action potential duration. In particular, we do not have one but instead several alternans modes having very distinct characteristics. The alternans mode frequencies are half integer multiples of the fundamental spiral wave rotation frequency (Ω). Interestingly, if one plots the time course of the membrane potential at a point fixed in the lab frame for any of the alternans modes, one observes patterns very similar to those of the single cell alternans mode independent of the mode frequency. Instead the higher frequency modes differentiate themselves from their lower frequency counterparts through the presence of short wavelength oscillations which are typical of what we refer to as discordant alternans [16,18,21,71,72].

An important consideration in this analysis is the effect of the finite system size [21,32,71] and the presence of the

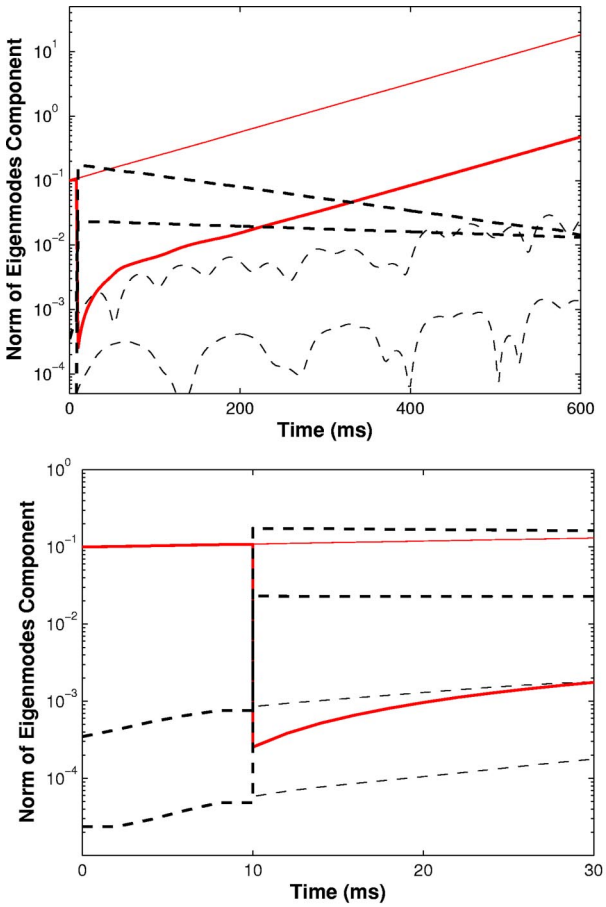

FIG. 9. (Color online) Time course of the amplitudes of selected eigenmodes for the simulations initialized with the specially chosen perturbation. Eigenmode amplitudes associated with the controlled case (stimulus applied at $t=10$ ms) are shown as thick lines; the uncontrolled case eigenmode amplitudes are plotted as thin lines. The lower panel shows the first 30 ms of the upper panel in greater detail. The amplitudes of one of the unstable alternans modes and two stable modes are shown as solid red and dashed black lines, respectively, for both the controlled and uncontrolled cases.

boundary on the stability and structure of the modes. To address this issue, we conducted a brief study in which the system radius was varied from 1.8 cm to a maximum of 6 cm. We observe that there are indeed some modifications in mode structure as the system size is varied, although the overall mode structure remains qualitatively the same. We find that the alternans modes become more unstable as the system size is increased. However, the alternans mode frequencies remain nearly constant at values that are half-integer multiples of the rotation frequency, strongly suggesting that the modes are governed primarily by alternans dynamics, independent of system size. Clearly, this issue requires further investigation, which we plan for the future.

An examination of the relative amplitudes of the perturbations on the wavefronts and wavebacks of the spiral waves suggests that two different mechanisms may exist for alternans in spiral waves. For Alternans Mode 3, the perturbation amplitude is large along the spiral wavefront whereas those of Alternans Modes 1 or 2 are larger along the waveback (see Fig. 4). Since the velocity of the wavefront is directly related to the upstroke dynamics [30], we can reasonably speculate that, in contrast to Modes 1 and 2, conduction velocity plays a significant role in the perturbation dynamics associated with Alternans Mode 3. Despite its known limitations [9,21,73], restitution theory has been a valuable tool that has helped improve our understanding of spiral wave dynamics [9,12,13,21,71]. In particular, it was found that CV dispersion can have an important effect on spiral wave breakup [9,12,16,21,71]. In our case, when the CV and APD restitution curves (which relate the APD and CV to the preceding diastolic interval DI) are plotted for a 1D cable composed of this type of cells, the steep part of the CV restitution curve occurs at DIs shorter than the value at which the slope of the APD restitution curve becomes greater than one (not shown). Since the latter is correlated with spiral wave instability, then for intermediate DIs, where the APD restitution curve has slope greater than one but the CV restitution curve is relatively flat, we would expect those modes driven by APD restitution to be unstable, whereas those dominated by CV variation to be stable. This is just the case illustrated in Fig. 4; here, Alternans Modes 1 and 2 are driven principally by steep APD restitution, as suggested by their large waveback perturbation amplitudes, and are found to be unstable (Fig. 2), whereas Alternans Mode 3 is stable, since it is dominated by CV variation, as suggested by its large wavefront perturbation amplitude. The situation changes when g_{fi} is increased, since this increases the rotation frequency, which shortens the steady state DI. In this case, we find that all three modes now have large wavefront perturbation amplitudes (not shown), suggesting all three are being influenced by CV variation dynamics. Since the CV restitution curve is steep for these values of DI, we can infer that, although APD restitution dynamics are still probably involved, all three are being driven more unstable by the dynamics of CV variation. Indeed, all three modes are unstable when g_{fi} is large [e.g., $g_{fi}=3.5$ (Fig. 5)]. Thus, as previously suggested [21], two mechanisms appear to exist, one dominated by APD restitution dynamics, and one in which CV and APD restitution both play significant roles.

Since substantial CV dispersion is necessary to initiate discordant alternans [71], which occurs at short DI in our case, it is also not surprising that in our study, higher frequency modes, i.e., discordant alternans, become dominant at high rotational frequency (see Fig. 5).

The example of control presented in the previous section introduces an important new approach towards the control of spiral wave breakup. A study by Echebarria *et al.* [53] showed that, in the context of their stimulus protocol, a single electrode cannot control alternans beyond a critical distance from the stimulus site. This would suggest that stimuli applied at a single location using this protocol might not be capable of controlling instabilities present in a large tissue. A similar limitation was found by Rappel *et al.* [49] in the control of wave breakup in 2D tissue. In contrast, our results, although obtained for a specialized case, demonstrate that a single stimulus applied at one instant in time *is* capable of controlling the amplitude of unstable perturbations over a large area, hundreds of square space constants in size, during almost five rotation periods of the spiral wave.

As can be seen in panel F of Fig. 8, it appears that, when the spiral wavefront first passes through the previously

stimulated region, the disturbance is picked up and amplified by the dynamics of the wavefront, and then propagates along both edges of the spiral wave (not shown). Such propagation is possible because the linear perturbation dynamics along these edges is active and highly unstable. This suggests that we might be able to improve stimulus protocols for controlling spiral wave instabilities by taking advantage of these active regions of spiral waves, rather than relying solely the diffusive property of the medium, as has been done previously [53,74]. One might therefore expect that a very efficient stimulus protocol may be possible, involving a minimal number of stimuli, that propagate their influence throughout the spiral wave by "surfing" the wave edges, bringing about major changes in the overall spatial and temporal dynamics of the entire wave.

The particular example of control presented in this paper is an extreme demonstration of the potential of the method, since the various unstable modes composing the perturbation were specifically chosen so as to allow their elimination with a single stimulus. For the more general case, we will probably need at least half as many stimuli as there are unstable modes, applied with different amplitudes at different times and/or different locations. Mathematically, this is explained by the necessity of satisfying as many conditions, as expressed in Eq. (15), as there are modes to be eliminated. This leads to solving a set of coupled equations with the timing and amplitudes of the stimuli being the unknowns. We have a lot of freedom in choosing the locations and the timing of the stimuli. Choosing the proper, most efficient and most practical control protocol may require the use of an optimization scheme, employing concepts and tools from control theory and a deeper understanding of the physiology and dynamics of the spiral wave alternans than can be obtained using perturbation theory by itself. This is beyond the scope of this paper and will be the focus of future studies. The main purpose here is rather to demonstrate the potential of perturbation theory, and to introduce new concepts discovered through its use in identifying active properties of the spiral wave as a whole, to control spiral wave breakup efficiently.

A number of limitations of our approach must be stated. First the 3V-SIM, does not reproduce properly some of the detailed ionic processes, and the action potential shape of more advanced ionic models, which have been shown to have noticeable effects on spiral wave stability [9,19,75]. Thus particular caution must be exercised when drawing conclusions on the electrophysiological characteristics of the various modes and their role in spiral wave stability when using 3V-SIM. Most importantly, perturbation theory, as used here, is limited to the study of linear behavior, and is therefore theoretically only valid for small perturbations. However insights obtained using the analogous method, when applied to the study and control alternans in single cells, have been shown to have application in both the linear and nonlinear regimes, and thereby have produced very promising results [68]. There is, of course, a long way to go before the method can be useful in practical application. The control schemes suggested here presuppose knowledge of each eigenmode composing the perturbation, which is not possible to obtain in practice. The method also assumes that the transition from tachycardia to fibrillation occurs smoothly and in an idealized rotating spiral wave, with a well defined center of rotation, initial conditions close to the steady state, in a homogeneous and isotropic tissue in two dimensions.

However despite all the limitations inherent to the theoretical approach of the study, we believe that linear perturbation theory will shed new light on the problem. A wealth of information can be extracted from the eigenvalue map and the eigenvectors structure. Future work will concentrate on exploiting this information to further study the physiological mechanism underlying alternans and spiral wave breakup, its possible relation to restitution theory, the effect of wavefront curvature, etc. We will pay particular attention to the extrapolation of results derived from the method (which are theoretically only valid for small perturbations) to the nonlinear regime. Studies employing perturbation theory could also be performed for more physiologically relevant sets of parameters of the 3V-SIM model (i.e., those that reproduce certain properties of the LRd, Beeler-Reuter, or other ionic models, etc.) than those used in this paper. Perturbation theory could also be applied to more advanced models.

This new approach may lead to new and useful concepts and properties of spiral waves that will also help in the design of practical electrical stimuli protocols or drug therapies. Our results suggest, for example, that stimuli should be applied in the resting state and close to the core for optimal efficiency. Our studies also suggest that a single or a few localized stimuli at one instant in time can control the alternans at distances much greater than the space constant. The characteristic frequencies and general spatial structure of the alternans modes we have found may also lead to new strategies for the design of control protocols that use modulated continuous stimuli at defined frequencies.

ACKNOWLEDGMENTS

This work was supported by the Whitaker Development Award (3426162). We are grateful to V. Hakim, H. Henry, D. Christini, D. Gauthier, and A. Karma for valuable discussions. Many of these occurred at the Workshop for Biological Excitable Media, at the Aspen Center for Physics, Aspen, CO, August 26 to September 8, 2002.

APPENDIX A: MODIFICATIONS TO THE 3V-SIM FENTON-KARMA MODEL

We found it necessary to make modifications to the 3V-SIM Fenton-Karma equations, so that they could be used with the Newton-Raphson method. The latter, which was employed in finding the steady state spiral wave, generally requires differentiable functions for convergence. We therefore replaced the Heaviside functions in the original equations with sigmoidal functions defined as $\mathcal{S}(u)=(1+\tanh(k_u u))/2$, where k_u was set to 50. The notations used are the same as those used in Ref. [21]. Thus, u, v and w represent the membrane potential, and the fast inward and slow inward inactivation gates, respectively. The total ionic current is composed of the sum of three different ionic currents: the fast

inward (I_{fi}), the slow outward (I_{so}) and the slow inward (I_{si}) currents. The modified equations of the model are thus:

$$\partial_t u = \nabla \cdot (D \nabla u) - I_{fi}(u,v) - I_{so}(u) - I_{si}(u,w) \tag{A1}$$

$$\equiv \nabla \cdot (D \nabla u) + \mathcal{F}_u(u,v,w) \tag{A2}$$

$$\partial_t v = \mathcal{S}(u_c - u)\frac{(1-v)}{\tau_v^-(u)} - \mathcal{S}(u - u_c)\frac{v}{\tau_v^+} \tag{A3}$$

$$\equiv \mathcal{F}_v(u,v) \tag{A4}$$

$$\partial_t w = \mathcal{S}(u_c - u)\frac{(1-w)}{\tau_w^-} - \mathcal{S}(u - u_c)\frac{w}{\tau_w^+} \tag{A5}$$

$$\equiv \mathcal{F}_w(u,w) \tag{A6}$$

where the currents are

$$I_{fi}(u,v) = -\frac{v}{\tau_d}\mathcal{S}(u - u_c)(1-u)(u - u_c) \tag{A7}$$

$$I_{so}(u) = \frac{u}{\tau_o}\mathcal{S}(u_c - u) + \frac{1}{\tau_r}\mathcal{S}(u - u_c) \tag{A8}$$

$$I_{si}(u,w) = -\frac{w}{2\tau_{si}}(1 + \tanh(k(u - u_{csi}))) \tag{A9}$$

where

$$\tau_v^-(u) = \mathcal{S}(u - u_v)\tau_{v2}^- + \mathcal{S}(u_v - u)\tau_{v1}^-. \tag{A10}$$

The parameters of the model were also modified. They were chosen to reduce instabilities caused by meandering while emphasizing alternans as a primary mechanism for breakup. The value for the parameters are as follows: $g_{fi}=1.75$, $\tau_r=33.83$, $\tau_{si}=29$, $\tau_o=12.5$, $\tau_v^+=7.99$, $\tau_{v2}^-=312.5$, $\tau_{v1}^-=9.8$, $\tau_w^+=870$, $\tau_w^-=41$, $u_c=0.13$, $u_v=0.04$, $u_{csi}=0.861$, $k=10$, $k_u=50$, and $D=0.002$ cm^2/ms with $\tau_d=c/g_{fi}$, where c the membrane capacitance per unit area is equal to 1 μF/cm^2. Note that the definition of τ_{v1}^- and τ_{v2}^- here and in Ref. [21] are interchanged compared to the definitions in Ref. [22]. Time is in units of ms and conductances in mS/cm^2. The membrane potential was normalized to 100 mV. Since the characteristic scale used with the sigmoid function was relatively short, simulation results using this model turned out to be very close to those obtained with the 3V-SIM Fenton-Karma model with discontinuous functions.

APPENDIX B: FINDING THE STEADY-STATE AND EXTRACTING THE DOMINANT EIGENVALUES

1. Finding the steady state

To find the steady state of the discretized version of Eq. (5), we used to a large extent the numerical approach presented by Henry and Hakim [40,41].

Using the Newton-Raphson method, we first find the steady state of a stable spiral wave having a circular core obtained with a reduced value for the conductance associated with the fast inward (sodium) current ($g_{fi}=1.4$) compared to the "standard" case. This is done by first creating a spiral wave in a square system discretized within a rectangular coordinate system, using the time and space discretized version of Eq. (3). The 9-point diffusion tensor is used to reduce effects associated with the anisotropy of the rectangular grid. The time advance is performed using the forward Euler method. The spiral wave is initiated using cross-field stimulation. Once the center of the core as well as the rotation frequency are found with reasonable accuracy, we transfer the spiral wave solution to a polar grid, where it is used as the initial guess to the Newton-Raphson convergence algorithm. In some cases, prior to transferring the spiral wave, the wave is allowed to rotate one extra time in a rectangular system from which cells in the four corners outside the eventual boundary of the new circular system are removed. This is done to lessen the impact of the change in boundary conditions between the two systems.

Given the initial guess $\boldsymbol{u}_1$, we would normally use the Newton-Raphson convergence method to solve iteratively the following relation for the $3N$ components of $\boldsymbol{u}_{k+1}$ given $\boldsymbol{u}_k$ (see Sec. II A 3 for the definition of $\boldsymbol{u}_k$):

$$H(\boldsymbol{u}_k)(\boldsymbol{u}_{k+1} - \boldsymbol{u}_k) = -G(\boldsymbol{u}_k). \tag{B1}$$

Iteration would continue until convergence to the desired steady state is obtained. Here k refers to the iteration number and G is the discretized version of $\mathcal{G}$ as defined in Eq. (4). The matrix $H(\boldsymbol{u})$ represents the Jacobian of G with respect to the components of $\boldsymbol{u}$, which is also equivalent to the discretized version of Eq. (7). The advective term is discretized in space according to the standard upwind-downwind paradigm [76] (which is possible, since the direction of advection is fixed by the rotation direction), while we use the usual second order finite differencing for the diffusion term. Matlab's standard matrix solver for sparse matrix equations is used to solve Eq. (B1) for $\boldsymbol{u}_{k+1}$.

Note, however, that there are actually $3N+1$ unknowns in these $3N$ equations, since the rotation frequency Ω is also unknown. Thus, we must modify the iterative equation (B1) to take this into account. Fortunately, due to the rotational symmetry of the problem, any solution that is rotated around the center point by any angle is also a steady state which results in an infinite number of solutions. We are, therefore, free to remove this ambiguity by fixing the membrane potential of one cell, reducing the number of unknowns back to $3N$. By choosing this value equal to 0.5, a value that typically occurs in the leading edge of the spiral wave, the solution with leading edge passing through this point will be found. We have found that this "anchoring" point is best chosen about two-thirds of the distance from the center, close to the location of the leading edge of the initial guess. Thus, the actual Jacobian matrix used in place of H in Eq. (B1) is the one obtained by assuming the independent variables are: Ω, and all the components of $\boldsymbol{u}$ except the membrane potential at the anchor point. This results in changes to one column in the matrix H as defined above. The function G in Eq. (B1) does not change.

With a properly chosen initial guess, the steady state spiral wave was obtained in less than 10 iterations to a precision of 10^{-10} as measured using the $\mathcal{L}_2$ norm of $G(u_0)$, $\|G(u_0)\|$. In polar coordinates, the $\mathcal{L}_2$ norm, $\|\boldsymbol{u}\|$, of $\boldsymbol{u}$, is defined as $\sqrt{\Sigma_{i=1}^{3N}|u^i|^2 S^i}$, where u^i refers to the ith element of $\boldsymbol{u}$ and S^i to the area of the cell associated with the ith grid point ($S^i \equiv \pi(\Delta r/2)^2$ for the central node and $S^i \equiv r^i \Delta r \Delta\theta$ otherwise).

Once the steady state is found for $g_{fi}=1.4$ for a stably rotating wave, g_{fi} was stepwise increased with the new steady state being calculated at each step. The steady state obtained for the previous value of g_{fi} was used as the initial guess for each new value of g_{fi}. This procedure was performed up to sodium conductance values for which the spiral wave breaks up.

2. Extracting the eigenvalues

The next step of the method consists of finding the eigenvalues of H evaluated for the steady state $\boldsymbol{u}_0$. Determination of the dominant eigenmodes (i.e., those eigenmodes with the largest growth rates, or largest real part of the eigenvalues) is not a simple task, due to the immense size of the matrix H ($3N$ by $3N$, or about 180 000 by 180 000). To handle this problem, we use a method presented by Henry and Hakim [40,41]. The idea is to use the Arnoldi method [69] to build an approximation to the subspace $\mathcal{E}_s$ spanned by the N_s most dominant eigenmodes. The eigenvalues and eigenvectors of interest are then easily obtained by projecting H onto this approximation of the subspace $\mathcal{E}_s$. Let us consider the method in more detail.

In this section, we will define $\mathcal{K}_{N_s}(H,\boldsymbol{u})$, the Krylov space of dimension N_s defined by the matrix H and the vector $\boldsymbol{u}$, as being $span(\boldsymbol{u}, H\boldsymbol{u}, H^2\boldsymbol{u}, \ldots, H^{N_s}\boldsymbol{u})$. It can be shown that a large enough Krylov subspace of any matrix H can yield the dominant eigenmodes of H with great accuracy. To obtain these eigenmodes, we create an orthogonal basis $(\boldsymbol{X})_{N_s} \equiv (\boldsymbol{X}_m)_{m=1,\ldots,N_s}$ for the subspace $\mathcal{K}_{N_s}(e^{Ht_1}, \boldsymbol{X}_1)$ using the Arnoldi method, where t_1 is a suitably chosen real constant. Note that e^{Ht_1} and H have the same eigenvectors while, if λ_m are the eigenvalues of H, the eigenvalues of e^{Ht_1} are simply $e^{\lambda_m t_1}$. By using the matrix e^{Ht_1} rather than H itself in the Arnoldi method [69], we can more easily eliminate the contribution of the more heavily damped modes and obtain an accurate approximation of the subspace $\mathcal{E}_s$ using a relatively low dimensional Krylov subspace.

We obtain an orthonormal basis using the Arnoldi method as follows. Having the first j orthonormalized vectors of the basis $(\boldsymbol{X})_j \equiv (\boldsymbol{X}_m)_{m=1,\ldots,j}$, we construct the next vector $\boldsymbol{X}_{j+1}$ by first calculating $\boldsymbol{Y}_j = e^{Ht_1}\boldsymbol{X}_j$, and then orthonormalizing it with respect to the rest of the basis by defining:

$$\boldsymbol{X}_{j+1} = \frac{\boldsymbol{Y}_j - \sum_{i=1}^{j} \langle \boldsymbol{Y}_j, \boldsymbol{X}_i \rangle \boldsymbol{X}_i}{\left\| \boldsymbol{Y}_j - \sum_{i=1}^{j} \langle \boldsymbol{Y}_j, \boldsymbol{X}_i \rangle \boldsymbol{X}_i \right\|}. \tag{B2}$$

The first vector $\boldsymbol{X}_1$ is obtained using a random initial condition $\boldsymbol{X}_0$ and calculating $\boldsymbol{X}_1 = e^{Ht_0}\boldsymbol{X}_0$. This first operation ensures that we are eliminating all unwanted, heavily damped eigenmodes. Similarly, the orthonormalization of the basis performed at each step of the Arnoldi method minimizes the increasing contribution of the most dominant modes of $\mathcal{E}_s$ coming from repeated applications of the operator H. The less dominant modes of $\mathcal{E}_s$ and therefore $\mathcal{E}_s$ itself can then be obtained with greater accuracy.

Once the orthonormalized basis $(\boldsymbol{X})_{N_s}$ is obtained, we calculate the matrix P, defined as the projection of e^{Ht_1} onto $\mathcal{K}_{N_s}(e^{Ht_1}, \boldsymbol{X}_1)$. The elements of the matrix P come from the various combinations of $\langle (\boldsymbol{Y})_{N_s}, (\boldsymbol{X})_{N_s} \rangle$ where the vectors $(\boldsymbol{Y})_{N_s}$ as defined earlier, were obtained during the Arnoldi process. The eigenvalues of P are just $e^{\lambda_m t_1}$ where the λ_m are the eigenvalues of the projection of H onto $\mathcal{K}_{N_s}(H, \boldsymbol{X}_1)$. These λ_m are approximations (albeit very good ones) to the leading eigenvalues of H. Since P is of dimension $N_s \times N_s$ with N_s typically chosen much smaller than $3N$ (on the order of 100), its eigenvalues can be easily calculated using conventional methods. Since H and e^{Ht_1} have the same eigenvectors, so do their projections onto the subspace $\mathcal{K}_{N_s}(e^{Ht_1}, \boldsymbol{X}_1)$. The eigenvectors $\boldsymbol{a}_m$ associated with λ_m can then be obtained from the eigenvectors associated with P denoted $\boldsymbol{b}_m$ by transferring the eigenvectors $\boldsymbol{b}_m$ from the $(\boldsymbol{X})_{N_s}$ basis onto the original basis of H. Explicitly, $\boldsymbol{a}_m = Q\boldsymbol{b}_m$, where Q is a $3N \times N_s$ matrix whose columns are filled with the vectors $\boldsymbol{X}_m$.

The accuracy of the method depends on the choice of t_0, t_1, the size of the subspace and the timestep. Typically we used a space of dimension $N_s=100$, a time duration $t_0 = 20$ ms and $t_1 = 10$ ms. The operator e^{Ht_1} is approximated by integrating, $\partial_t \delta\boldsymbol{u} = \boldsymbol{\mathcal{D}}(\boldsymbol{\mathcal{G}}(\boldsymbol{u}_0))\delta\boldsymbol{u}$ [Eq. (6)], for time duration t_1 using the simulation method described in Sec. II A 1. The advection term is handled using a standard upwind-downwind method. The timestep was chosen to be 0.001 ms to obtain the first vector of the basis $(\boldsymbol{X})_{N_s}$ and 0.01 ms for all the other vectors. A smaller value of timestep was necessary for the first vector in order to have enough iterations to allow the high spatial discontinuity in u, v, and w associated with the random nature of the initial condition to dissipate. This was increasingly important toward the center, due to the very fine grid size used in the azimuthal direction. Using these parameters values, we were able to obtain an accuracy of $\|(H\boldsymbol{a}_m - \lambda_m \boldsymbol{a}_m)/\lambda_m\| < 10^{-8}$ for the first 10 and $<10^{-4}$ for the next 5 eigenmodes. This resulted in less than 1% error for the value $\max(|H\boldsymbol{a}_m - \lambda_m \boldsymbol{a}_m|)/\max(|\lambda_m \boldsymbol{a}_m|)$ for the 10 first eigenmodes. Note that the eigenvectors are all normalized to 1 using the $\mathcal{L}_2$ norm.

APPENDIX C: LEFT EIGENVECTORS AND ADJOINT OPERATOR

The left eigenvectors are defined to be the eigenvectors of the adjoint of the matrix H as defined in Appendix B. The adjoint of H, $H^\dagger$, is defined relative to the inner product in polar coordinates, $\langle , \rangle$ given by Eq. (12). In this appendix, we show how to obtain the left eigenvectors and we describe useful properties they have with respect to the right eigenvectors.

Let us define a diagonal matrix S for which each element S^{ii} of the diagonal is equal to the surface of the grid element

associated with the ith variable. We therefore have that $S^{ii} = r^i \Delta r \Delta\theta$ (Δr and $\Delta\theta$ are the grid spacing in r direction and angle step in azimuthal direction), except at the center where $S^{ii} = \pi \Delta r^2/4$. For convenience, we will define $S^i \equiv S^{ii}$.

The inner product in polar coordinates as defined by Eq. (12) between the vectors $\boldsymbol{x}$ and $\boldsymbol{y}$ may then be written as, $\langle \boldsymbol{x}, \boldsymbol{y} \rangle = \boldsymbol{x}^* \cdot (S\boldsymbol{y}) = (\boldsymbol{x}^* S^*) \cdot \boldsymbol{y} = \sum_{i=1}^{3N} \overline{x^i} y^i S^i$, where * refers to the conjugate transpose operator ($\boldsymbol{x}^* \equiv \overline{\boldsymbol{x}^T}$). Defining $H^\dagger$ to be the adjoint matrix associated with this inner product, we then have, by definition:

$$\langle \boldsymbol{y}, H\boldsymbol{x} \rangle \equiv \langle H^\dagger \boldsymbol{y}, \boldsymbol{x} \rangle \tag{C1}$$

$$= \boldsymbol{y}^* \cdot (SH\boldsymbol{x}) \tag{C2}$$

$$= \boldsymbol{y}^* \cdot (SHS^{-1}S\boldsymbol{x}) \tag{C3}$$

$$= (\boldsymbol{y}^* ((S^{-1})^* H^* S^*)^*) \cdot S\boldsymbol{x} \tag{C4}$$

$$= (S^{-1} H^* S\boldsymbol{y})^* \cdot S\boldsymbol{x}. \tag{C5}$$

However H^* is equal to the transpose of H ($H^* = H^T$) since H is real. Consequently, the adjoint of H is given by:

$$H^\dagger = S^{-1} H^* S = S^{-1} H^T S \tag{C6}$$

When solving the eigenvalue problem, we obtain $3N$ eigenmodes $\boldsymbol{a}_m$ and associated eigenvalues λ_m for H such that $H\boldsymbol{a}_m = \lambda_m \boldsymbol{a}_m$. Similarly, we have the left eigenvectors $\tilde{\boldsymbol{a}}_m$ associated with $H^\dagger$. Since H^T and H have the same set of eigenvalues, so does $S^{-1}H^T S$, since they all have the same characteristic polynomial. Therefore, from Eq. (C6), we can infer that H and $H^\dagger$ have the same set of eigenvalues (but different vectors), as expected. For any pair of right and left eigenvectors $\boldsymbol{a}_m$ and $\tilde{\boldsymbol{a}}_n$, we have:

$$\langle \tilde{\boldsymbol{a}}_n, H\boldsymbol{a}_m \rangle = \lambda_m \langle \tilde{\boldsymbol{a}}_n, \boldsymbol{a}_m \rangle \tag{C7}$$

$$= \langle H^\dagger \tilde{\boldsymbol{a}}_n, \boldsymbol{a}_m \rangle \tag{C8}$$

$$= \overline{\lambda_n} \langle \tilde{\boldsymbol{a}}_n, \boldsymbol{a}_m \rangle. \tag{C9}$$

This implies that either $\overline{\lambda_n} = \lambda_m$ or $\langle \tilde{\boldsymbol{a}}_n, \boldsymbol{a}_m \rangle = 0$. In other words, those left eigenvectors with eigenvalues distinct from λ_m are each perpendicular to the right eigenvectors associated with λ_m. We, therefore, define the left eigenvector and its associated eigenvalue $(\tilde{a}_m, \overline{\lambda_m})$ to be the left eigenmode associated with the right eigenmode (a_m, λ_m) by assigning each the same subscript m.

The left eigenvectors are easily calculated by first finding the eigenvalues γ_m and corresponding right eigenvectors $\boldsymbol{c}_m$ of H^T. From Eq. (C6), we then see that the left eigenvectors may be calculated using the relation $\tilde{\boldsymbol{a}}_m = S^{-1}\boldsymbol{c}_m$, while corresponding eigenvalues are $\overline{\lambda_m} = \gamma_m$.

[1] D. P. Zipes and H. J. J. Wellens, Circulation **98**, 2334 (1998).
[2] A. T. Winfree, Chaos **1**, 303 (1991).
[3] A. Pertsov, J. Davidenko, R. Salomonsz, W. Baxter, and J. Jalife, Circ. Res. **72**, 631 (1993).
[4] J. Davidenko, A. Pertsov, R. Salomonsz, W. Baxter, and J. Jalife, Nature (London) **355**, 349 (1992).
[5] R. A. Gray, A. M. Pertsov, and J. Jalife, Nature (London) **392**, 75 (1998).
[6] M. L. Walker and D. S. Rosenbaum, Cardiovasc. Res. **57**, 599 (2003).
[7] E. Cytrynbaum and J. P. Keener, Chaos **12**, 788 (2002).
[8] F. H. Samie and J. Jalife, Cardiovasc. Res. **50**, 242 (2001).
[9] E. M. Cherry and F. H. Fenton, Am. J. Physiol. **286**, H2332 (2004).
[10] P. S. Chen, T. J. Wu, C. T. Ting, H. S. Karagueuzian, A. Garfinkel, S. F. Lin, and J. N. Weiss, Circulation **108**, 2298 (2003).
[11] I. Banville and R. A. Gray, J. Cardiovasc. Electrophysiol. **13**, 1141 (2002).
[12] T. J. Wu, S. F. Lin, J. N. Weiss, C. T. Ting, and P. S. Chen, Circulation **106**, 1859 (2002).
[13] A. Garfinkel, Y. H. Kim, O. Voroshilovsky, Z. L. Qu, J. R. Kil, M. H. Lee, H. S. Karagueuzian, J. N. Weiss, and P. S. Chen, Proc. Natl. Acad. Sci. U.S.A. **97**, 6061 (2000).
[14] J. M. Pastore, S. D. Girouard, K. R. Laurita, F. G. Akar, and D. S. Rosenbaum, Circulation **99**, 1385 (1999).
[15] H. M. Hastings, F. H. Fenton, S. J. Evans, O. Hotomaroglu, J. Geetha, K. Gittelson, J. Nilson, and A. Garfinkel, Phys. Rev. E **62**, 4043 (2000).
[16] M. Courtemanche, Chaos **6**, 579 (1996).
[17] I. R. Efimov, V. I. Krinsky, and J. Jalife, Chaos, Solitons Fractals **5**, 513 (1995).
[18] Z. L. Qu, F. G. Xie, A. Garfinkel, and J. N. Weiss, Ann. Biomed. Eng. **28**, 755 (2000).
[19] J. J. Fox, E. Bodenschatz, and R. F. Gilmour, Phys. Rev. Lett. **89**, 138101 (2002).
[20] A. V. Panfilov, Phys. Rev. Lett. **88**, 118101 (2002).
[21] F. H. Fenton, E. M. Cherry, H. M. Hastings, and S. J. Evans, Chaos **12**, 852 (2002).
[22] F. Fenton and A. Karma, Chaos **8**, 20 (1998).
[23] E. Chudin, A. Garfinkel, J. Weiss, W. Karplus, and B. Kogan, Prog. Biophys. Mol. Biol. **69**, 225 (1998).
[24] Z. L. Qu, J. N. Weiss, and A. Garfinkel, Am. J. Physiol. **45**, H269 (1999).
[25] F. G. Xie, Z. L. Qu, A. Garfinkel, and J. N. Weiss, Am. J. Physiol. **280**, H1667 (2001).
[26] T. J. Hund, N. F. Otani, and Y. Rudy, Am. J. Physiol. **279**, H1869 (2000).
[27] M. Courtemanche, L. Glass, and J. P. Keener, Phys. Rev. Lett. **70**, 2182 (1993).
[28] B. Echebarria and A. Karma, Phys. Rev. Lett. **88**, 208101 (2002).
[29] P. Comtois and A. Vinet, Phys. Rev. E **68**, 051903 (2003).
[30] J. J. Tyson and J. P. Keener, Physica D **32**, 327 (1988).
[31] V. Hakim and A. Karma, Phys. Rev. Lett. **79**, 665 (1997).
[32] V. Hakim and A. Karma, Phys. Rev. E **60**, 5073 (1999).

[33] D. Margerit and D. Barkley, Phys. Rev. E **66**, 036214 (2002).
[34] M. Li and N. F. Otani, Ann. Biomed. Eng. **31**, 1213 (2003).
[35] J. Beaumont, N. Davidenko, J. M. Davidenko, and J. Jalife, Biophys. J. **75**, 1 (1998).
[36] P. Comtois and A. Vinet, Phys. Rev. E **60**, 4619 (1999).
[37] D. Barkley, Phys. Rev. Lett. **68**, 2090 (1992).
[38] D. Barkley, Phys. Rev. Lett. **72**, 164 (1994).
[39] N. F. Otani, Chaos **12**, 829 (2002).
[40] H. Henry and V. Hakim, Phys. Rev. E **65**, 046235 (2002).
[41] H. Henry and V. Hakim, Phys. Rev. Lett. **85**, 5328 (2000).
[42] A. Karma, Phys. Rev. Lett. **71**, 1103 (1993).
[43] D. S. Rosenbaum, L. E. Jackson, J. M. Smith, H. Garan, J. N. Ruskin, and R. J. Cohen, N. Engl. J. Med. **330**, 235 (1994).
[44] M. L. Koller, M. L. Riccio, and R. F. Gilmour, Am. J. Physiol. **44**, H1635 (1998).
[45] C. A. S. T. C. Investigators, N. Engl. J. Med. **321**, 406 (1989).
[46] C. A. S. T. C. I. Investigators, N. Engl. J. Med. **327**, 227 (1992).
[47] A. L. Waldo, A. J. Camm, H. deRuyter, P. L. Friedman, D. J. MacNeil, J. F. Pauls, B. Pitt, C. M. Pratt, P. J. Schwartz, and E. P. Veltri, Lancet **348**, 7 (1996).
[48] D. J. Gauthier, G. M. Hall, R. A. Oliver, E. G. Dixon-Tulloch, P. D. Wolf, and S. Bahar, Chaos **12**, 952 (2002).
[49] W. J. Rappel, F. Fenton, and A. Karma, Phys. Rev. Lett. **83**, 456 (1999).
[50] K. Hall, D. J. Christini, M. Tremblay, J. J. Collins, L. Glass, and J. Billette, Phys. Rev. Lett. **78**, 4518 (1997).
[51] G. M. Hall and D. J. Gauthier, Phys. Rev. Lett. **88**, 198102 (2002).
[52] S. Alonso, F. Sagues, and A. S. Mikhailov, Science **299**, 1722 (2003).
[53] B. Echebarria and A. Karma, Chaos **12**, 923 (2002).
[54] D. J. Christini, K. M. Stein, S. M. Markowitz, S. Mittal, D. J. Slotwiner, M. A. Scheiner, S. Iwai, and B. B. Lerman, Proc. Natl. Acad. Sci. U.S.A. **98**, 5827 (2001).
[55] A. T. Stamp, G. V. Osipov, and J. J. Collins, Chaos **12**, 931 (2002).
[56] H. Zhang, B. B. Hu, and G. Hu, Phys. Rev. E **68**, 026134 (2003).
[57] R. A. Gray, Chaos **12**, 941 (2002).
[58] V. Krinsky, F. Plaza, and V. Voignier, Phys. Rev. E **52**, 2458 (1995).
[59] P. Comtois and A. Vinet, Chaos **12**, 903 (2002).
[60] P. Y. Wang, P. Xie, and H. W. Yin, Chin. Phys. **12**, 674 (2003).
[61] S. Sinha, K. M. Stein, and D. J. Christini, Chaos **12**, 893 (2002).
[62] R. Pandit, A. Pande, S. Sinha, and A. Sen, Physica A **306**, 211 (2002).
[63] G. V. Osipov, B. V. Shulgin, and J. J. Collins, Phys. Rev. E **58**, 6955 (1998).
[64] V. N. Biktashev and A. V. Holden, J. Electrocardiol. **32**, 76 (1999).
[65] V. N. Biktashev and A. V. Holden, Chaos **8**, 48 (1998).
[66] S. Sinha, A. Pande, and R. Pandit, Phys. Rev. Lett. **86**, 3678 (2001).
[67] M. Li and N. F. Otani, Biophys. J. **82**, 92D (2002) (Supplement).
[68] M. Li and N. F. Otani, Ann. Biomed. Eng. **32**, 784 (2004).
[69] Y. Saad, *Iterative methods for sparse linear systems* (PWS, Boston, 1996).
[70] See EPAPS Document No. E-PLEEE8-70-076411 for movies associated with Figs. 1, 3, 4, and 8. A direct link to this document may be found in the online article's HTML reference section. The document may also be reached via the EPAPS homepage (http://www.aip.org/pubservs/epaps.html) or from ftp.aip.org in the directory /epaps/. See the EPAPS homepage for more information.
[71] M. A. Watanabe, F. H. Fenton, S. J. Evans, H. M. Hastings, and A. Karma, J. Cardiovasc. Electrophysiol. **12**, 196 (2001).
[72] A. Goryachev and R. Kapral, Phys. Rev. Lett. **76**, 1619 (1996).
[73] R. F. Gilmour, J. Cardiovasc. Electrophysiol. **13**, 1150 (2002).
[74] W. J. Rappel, Chaos **11**, 71 (2001).
[75] F. H. Fenton, S. J. Evans, and H. M. Hastings, Phys. Rev. Lett. **83**, 3964 (1999).
[76] L. N. Trefethen, *Numerical linear algebra* (Society for Industrial and Applied Mathematics, Philadelphia, 1997).